

ORIGINAL ARTICLE

Open Access



Influence of Cavitation on Unsteady Vortical Flows in a Side Channel Pump

Yefang Wang¹, Fan Zhang^{1*} , Shouqi Yuan¹, Ke Chen¹, Feng Hong² and Desmond Appiah¹

Abstract

Previous investigation on side channel pump mainly concentrates on parameter optimization and internal unsteady vortical flows. However, cavitation is prone to occur in a side channel pump, which is a challenging issue in promoting performance. In the present study, the cavitating flow is investigated numerically by the turbulence model of SAS combined with the Zwart cavitation model. The vapors inside the side channel pump firstly occur in the impeller passage near the inlet and then spread gradually to the downstream passages with the decrease of NPSHa. Moreover, a strong adverse pressure gradient is presented at the end of the cavity closure region, which leads to cavity shedding from the wall. The small scaled vortices in each passage reduce significantly and gather into larger vortices due to the cavitation. Comparing the three terms of vorticity transport equation with the vapor volume fraction and vorticity distributions, it is found that the stretching term is dominant and responsible for the vorticity production and evolution in cavitating flows. In addition, the magnitudes of the stretching term decrease once the cavitation occurs, while the values of dilatation are high in the cavity region and increase with the decreasing NPSHa. Even though the magnitude of the baroclinic torque term is smaller than vortex stretching and dilatation terms, it is important for the vorticity production along the cavity surface and near the cavity closure region. The pressure fluctuations in the impeller and side channel tend to be stronger due to the cavitation. The primary frequency of monitor points in the impeller is 24.94 Hz and in the side channel is 598.05 Hz. They are quite corresponding to the shaft frequency of 25 Hz ($f_{\text{shaft}} = 1/n = 25$ Hz) and the blade frequency of 600 Hz ($f_{\text{blade}} = Z/n = 600$ Hz) respectively. This study complements the investigation on cavitation in the side channel pump, which could provide the theoretical foundation for further optimization of performance.

Keywords Side channel pump, Vortical flows, Cavitation, Vortex-cavitation interaction, Pressure fluctuation

1 Introduction

Side channel pump is a kind of radial vane pump between positive displacement pumps and centrifugal pumps, which has a semicircular side channel on the axial side of the impeller [1]. The specific speed of side channel pumps is lower and the size is smaller than traditional centrifugal pumps. The fluid in side channel pump flows from an

impeller passage to the side channel and then returns to the next impeller passage. It then flows out of the pump through one circulation to the next and the whole movement follows a helical path [2–5]. Due to the flow in the helical path, there are strong swirling flows and numerous vortex structures in the side channel pump. Meanwhile, as the pressure near the vortex core region is very low, the cavitation is much more easily induced than traditional centrifugal pumps. Therefore, further investigation of the characteristics of the cavitation in the side channel need to be done to improve the performance and reduce instabilities.

Cavitation is the hydrodynamic phenomenon of liquid vaporization due to local drop of static pressure and

*Correspondence:

Fan Zhang
fzhang@ujs.edu.cn

¹ National Research Center of Pumps, Jiangsu University, Zhenjiang 212013, China

² College of Mechanical & Power Engineering, China Three Gorges University, Yichang 443002, China

it is commonly associated with adverse effects, such as performance degradation, pressure fluctuation, noise, vibration and erosion [6, 7]. Due to the importance of cavitation effect, abundant researches have been conducted to investigate the cavitating flows in recent years. Fu et al. [8] investigated the characteristics of flow instabilities and cavitation in a centrifugal pump at low flow rates by experimental and numerical methods. It was found that the low frequency pressure fluctuations were related to the flow instabilities induced by the occurrence of cavitation at low flow rates. Lu et al. [9] studied the cavitating flows in a low specific speed model pump-turbine by experiments and found that the occurrence of the rotating stall was influenced greatly by the variation of cavitation number while the pressure fluctuation frequency caused by rotating stall did not vary significantly. Although the results tested by experiments are more reliable, the detailed information of internal cavitating flows is hard to be measured and obtained as the limitation of experimental conditions. Therefore, numerical methods play an important role in investigating the cavitation characteristics with the development of computational fluid dynamics. For simulating the cavitation accurately, the choice of turbulence model is critical in predicting the unsteady behavior of cavitating flows. Delgosha et al. [10] proposed the density-correction method (DCM) and used the modified RNG k - ε turbulence model coupled with a homogenous cavitation model to simulate partial cavitation on a 2D venturi nozzle. They observed the time-averaged velocity profiles in the turbulent cavity closure region showed some discrepancies with the experiment. This can be attributed to the fact that the capability of the Reynolds averaged Navier-Stokes (RANS) models with eddy viscosity turbulence models to simulate unsteady cavitating flows is limited due to its over-prediction of eddy viscosity. Large eddy simulation (LES) is a reliable method but it is computationally extremely costly in engineering applications. Therefore, the hybrid RANS-LES models have been popular recently, which is an efficient approach to reduce the computational cost and improve simulation accuracy. Tan et al. [11] modified the renormalization group (RNG) by the filter-based model (FBM) to simulate the cavitating flow in a centrifugal pump at a low flow rate. The results revealed that the calculated cavitation performance curve agreed well with the experimental measurements and the pressure fluctuation induced by cavitation was stronger than that of non-cavitation condition. Ennouri et al. [12] investigated the centrifugal pump by scale-adapted simulation (SAS) through non-cavitation and cavitation conditions and the results showed an acceptable agreement with testing data. On the other hand, an effective cavitation model is another fundamental technique for CFD research

of cavitation, which can describe the interphase mass transfer between the liquid and vapor phases. In recent years, many transport equation models, belonging to the homogenous models, have been developed by solving the mass transport between two phases with the vaporization and condensation source terms, such as Kunz et al. [13], Schnerr and Sauer [14], Zwart et al. [15] and Singhal et al. [16]. Each cavitation model has its advantages and they are widely applied in simulating the cavitating flows [17, 18].

Additionally, cavitation involves complex interactions of turbulence and phase-change dynamics, which is not only induced in vortical structures but is also a mechanism for vorticity generation [19]. However, the mechanism of the interaction between the vortex generation and cavitation is still a hard problem. This issue has been significantly investigated on the cavitating flows of hydrofoils [20–23]. These investigations provided insight into the cavitation-vortex interactions and indicated that the vorticity transport equation was a powerful tool for studying the interactions between cavitation and vortex structures. Cavitation can affect the characteristics of vortices [24] and lead to severe vibration [25], and it is validated that the dynamic behavior of the cavity is significantly related to the vortex structure. Besides, cavitation and vortex are interacting in the flow field, and the mechanism can be revealed by the vorticity transport equation. However, the vorticity transport equation has not been widely used to analyze the evolution of the cavitation and vortices in centrifugal pumps, especially in side channel pumps, due to the complexity of the internal flows. Therefore, the turbulence model of SAS combined with the Zwart cavitation model is employed to simulate the cavitating flow in the side channel pump with the accuracy validation by experimental data of Fleder [26]. This present investigation aims to elucidate the transient flow pattern, cavitation-vortex interaction, and pressure fluctuation, which may provide a better understanding of vortex cavitation in the side channel pump.

2 Pump Geometry and Mesh Generation

2.1 Parameters of Pump

Figure 1 shows the computational configuration of the side channel pump and the cross-section shape of the blade, includes four hydraulic components as suction pipe, impeller, side channel and discharge pipe. The design parameters of the pump with a specific speed n_s are as follows: $H = 13.5$ m, $Q = 10$ m³/h, $n = 1500$ r/min, $n_s = \frac{3.65nQ^{1/2}}{H^{3/4}} = 41$. The main geometrical parameters of the side channel pump are listed in Table 1, including impeller diameter $D_2=150$ mm, blade number $Z = 24$, blade suction angle $\theta = 10^\circ$ and side channel radius $R = 17.6$ mm. Moreover, the Reynolds number at

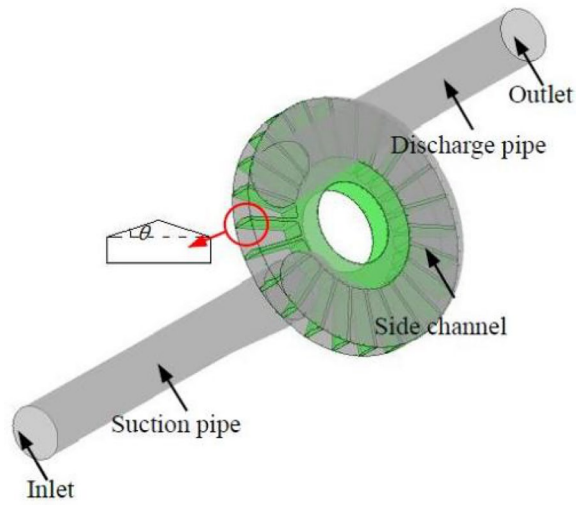


Figure 1 Flow configuration

Table 1 Geometric parameters

Parameters	Values
Impeller inlet diameter D_1 (mm)	80
Impeller outlet diameter D_2 (mm)	150
Blade width w (mm)	15
Blade thickness b (mm)	2
Blade suction angle θ (°)	10
Blade number Z	24
Radial gap σ (mm)	0.2
Axial gap S (mm)	0.2
Wrapping angle φ (°)	30
Side channel radius R (mm)	17.6

the inlet of the side channel pump $Re_{inlet} = \frac{\rho v_1 d_1}{\mu}$ is about 10^5 under the design condition, where v_1 and d_1 are the velocity and diameter of the inlet suction pipe.

2.2 Mesh Analysis

All computational domains are meshed with high-quality structured hexahedral multi-block grids, which were created in ICEM CFD. Critical regions such as the near-wall region (boundary layer) and the transition section (rotor-stator interfaces) were refined to capture the detailed flow characteristics. It should be noted that the length of suction and discharge pipes are extended to 5 times of pipe diameter to ensure the accuracy of simulations. If the distance is too short, convergence is very difficult because of reversed flow at the inlet and out boundaries.

Table 2 Grid independent analysis

Test grids	Mesh nodes ($\times 10^6$)	Mean value of y^+		Head (m)
		Impeller	Side channel	
Grid 1	4.43	16.9	27.3	12.129
Grid 2	6.11	12.3	26.3	12.236
Grid 3	8.01	6.7	26.2	12.426
Grid 4	9.19	6.1	26.2	12.422

Moreover, the fluid domains of radial and axial gaps are integrated with that of the impeller for reducing the negative effects of interfaces on the simulation accuracy. Similarly, the fluid domain of the discharge pipe is also integrated with that of the side channel. Interfaces are located between the suction pipe and the impeller as well as between the impeller and the side channel.

According to the previous investigation in the side channel pump [27], totally four sets of computational meshes are used to check the influence of mesh size on simulations and the grid independent results are as Table 2 shown. It is observed that the head of the model pump becomes stable gradually with the increase of the mesh nodes and the error between grid 3 and grid 4 is about 0.032%. Therefore, the third grid is chosen in this investigation and the structured hexahedral meshes of different components are shown in Figure 2. Moreover, the nondimensional distance from the wall y^+ could inspect the mesh quality near the boundary layer. The corresponding mean value of y^+ of impeller blades is about 6 while the magnitudes of y^+ don't exceed 30 for a large portion of the side channel, which is depicted in Figure 3.

3 Methodology of Numerical Simulations

3.1 Governing Equations

In the homogeneous assumption of the mixture of water and vapor in the cavity flow, the multiphase fluid components are assumed to same velocity and pressure fields. The continuity and momentum equations in the Cartesian coordinates are given below:

$$\frac{\partial \rho_m}{\partial t} + \frac{\partial (\rho_m u_i)}{\partial x_i} = 0, \quad (1)$$

$$\frac{\partial (\rho_m u_i)}{\partial t} + \frac{\partial (\rho_m u_i u_j)}{\partial x_j} = \frac{\partial p}{\partial x_i} + \frac{\partial}{\partial x_j} \left[(\mu_m + \mu_t) \left(\frac{\partial u_i}{\partial x_j} + \frac{\partial u_j}{\partial x_i} - \frac{2}{3} \frac{\partial u_k}{\partial x_k} \delta_{ij} \right) \right], \quad (2)$$

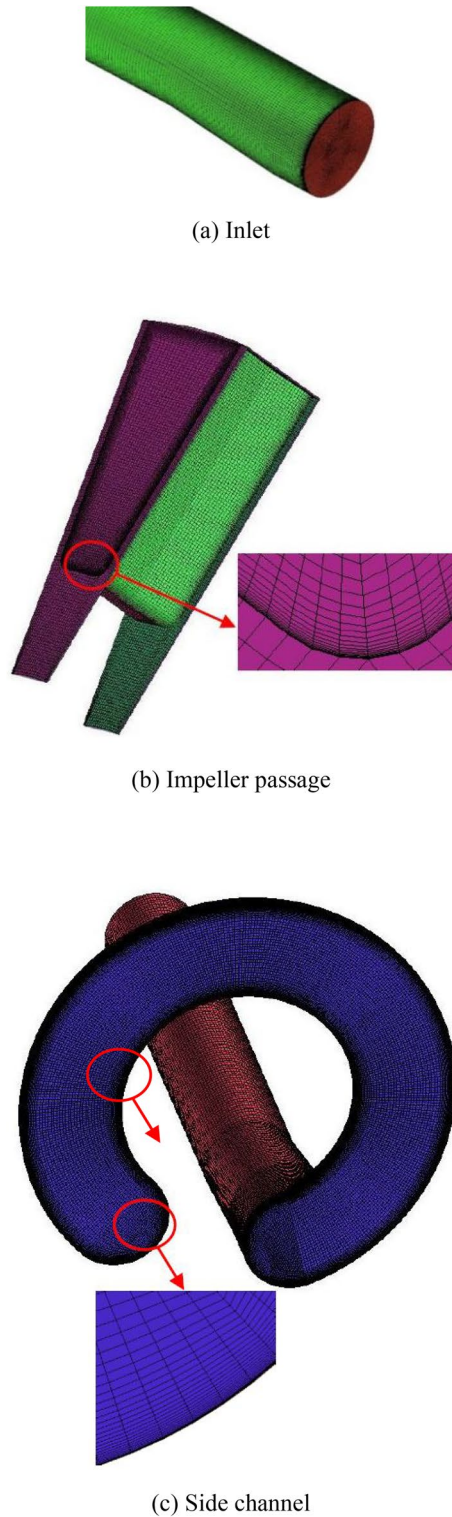


Figure 2 Detailed meshes of different components

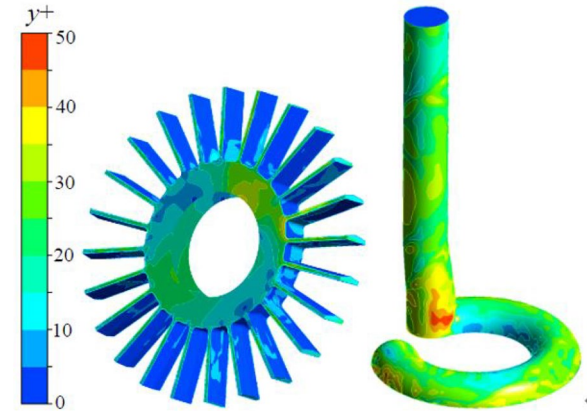


Figure 3 Distribution of y^+ on the surface of blades and side channel

where ρ_m is the mixture density, u is the velocity, p is the pressure, μ and μ_t are the laminar and turbulent viscosity, and subscripts i, j, k are the axes directions, respectively. The mixture density ρ_m is defined as $\rho_m = \alpha_l \rho_l + \alpha_v \rho_v$ and the mixture viscous is $\mu_m = \alpha_l \mu_l + \alpha_v \mu_v$, where the subscripts l and v , α is the volume fraction of one component.

3.2 Turbulence Model

The effect of different turbulence models on the internal flows was discussed in the previous investigation [27] and SAS is applied in this paper. Noticeably, SAS provides a continuous variation of solution ranging from LES-type to RANS-type with respect to the timestep corresponding to the CFL number selected in the simulation. The SST-SAS model modifies the turbulence frequency ω by the additional SAS source term Q_{SAS} when compared with SST-RANS model and it is defined as [28, 29]:

$$\frac{\partial(\rho k)}{\partial t} + \frac{\partial(\rho u_j k)}{\partial x_j} = P_k - \rho c_\mu k \omega + \frac{\partial}{\partial x_j} \left[\left(\mu + \frac{\mu_t}{\sigma_k} \right) \frac{\partial k}{\partial x_j} \right], \quad (3)$$

$$\begin{aligned} \frac{\partial(\rho \omega)}{\partial t} + \frac{\partial(\rho u_j \omega)}{\partial x_j} &= \alpha \frac{\omega}{k} P_k - \beta \rho \omega^2 + Q_{SAS} \\ &+ \frac{\partial}{\partial x_j} \left[\left(\mu + \frac{\mu_t}{\sigma_\omega} \right) \frac{\partial \omega}{\partial x_j} \right] + (1 - F_1) CD_{k\omega}. \end{aligned} \quad (4)$$

The additional source term Q_{SAS} is as below [28, 29]:

$$Q_{SAS} = \max \left[\rho \xi_2 k S^2 \left(\frac{L}{L_{vk}} \right)^2 - C_{SAS} \frac{2\rho k}{\sigma_\phi} \max \left(\frac{1}{k^2} \frac{\partial k}{\partial x_j} \frac{\partial k}{\partial x_j}, \frac{1}{\omega^2} \frac{\partial \omega}{\partial x_j} \frac{\partial \omega}{\partial x_j} \right), 0 \right], \quad (5)$$

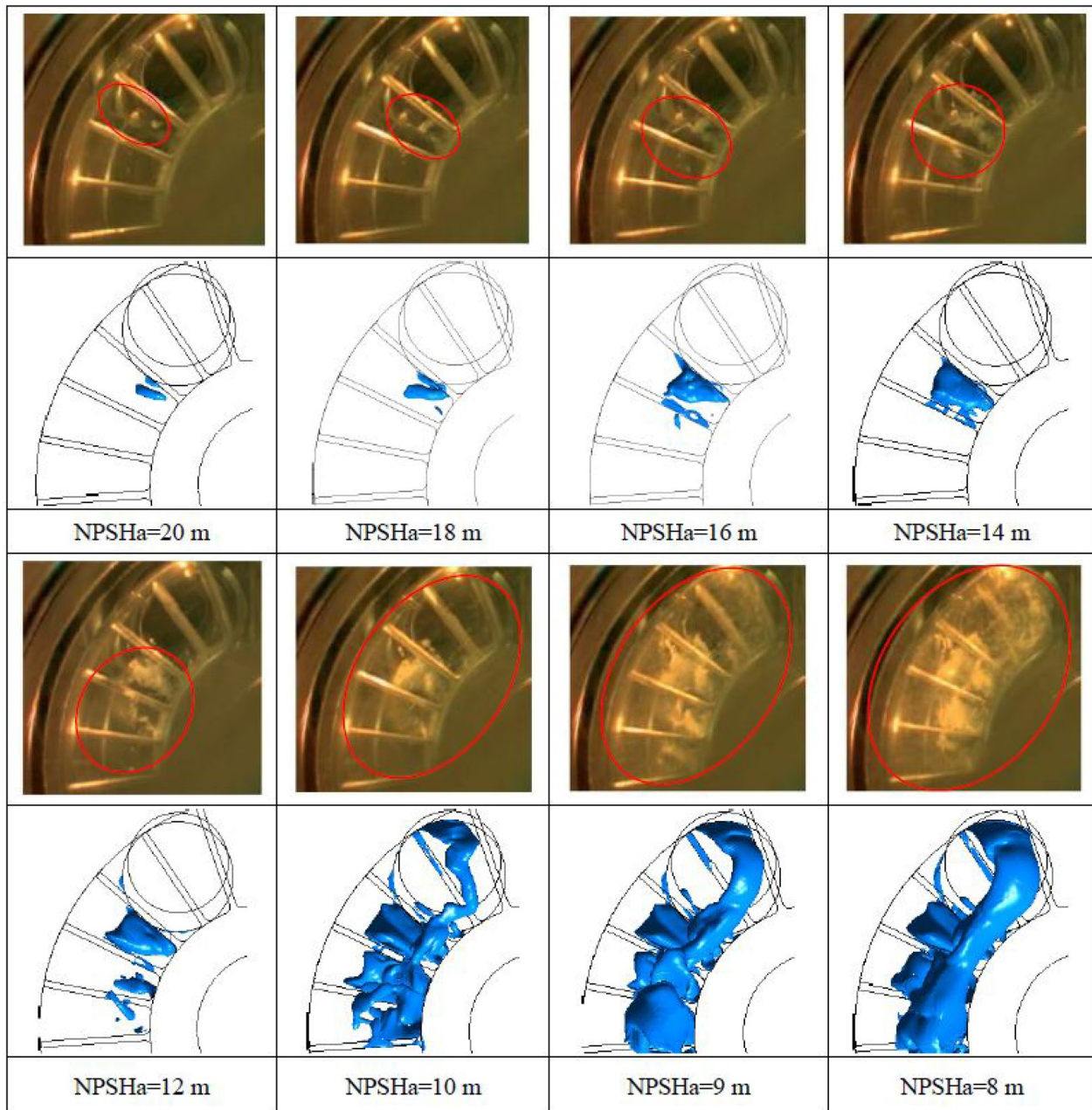


Figure 4 Comparisons of experimental photographs [26] and numerical cavity structures

where $\xi_2 = 3.51$, $C_{SAS} = 2$, $\sigma_\phi = \sigma_k = \frac{2}{3}$, L and L_{vk} are the modeled turbulence length scale and Von Karman length scale respectively and defined as $L = \sqrt{k}/c_\mu^{1/4}$,

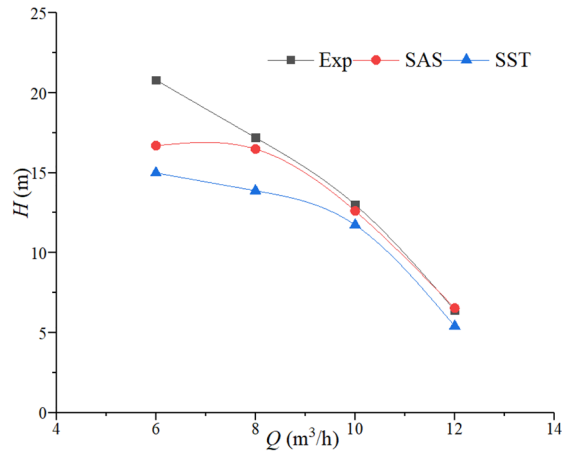
$$L_{vk} = \max \left(\left| \frac{k \sqrt{2S_{ij}S_{ij}}}{\sqrt{\nabla^2 U} \cdot \nabla^2 U} \right|, C_s \sqrt{\frac{k\eta_2}{(\beta/c_\mu)^{-\alpha}}} \cdot \Delta \right). \text{ Besides,}$$

the other terms in the ω equation in situation of unsteady flows are dominated by the additional source term Q_{SAS} , implying an increasing ω leading to a decrease of the

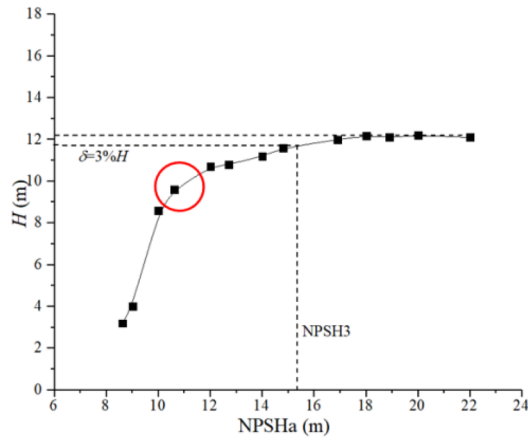
turbulent eddy viscosity since $\nu_t = k/\omega$. In addition, $CD_{k\omega} = \frac{2\rho}{\sigma\omega^2} \frac{1}{\omega} \frac{\partial k}{\partial x_j} \frac{\partial \omega}{\partial x_j}$ and F_1 is the blend function.

3.3 Cavitation Model

Based on the homogeneous flow theory, without accounting for the thermal energy and non-equilibrium phase change effects, the Zwart cavitation model derived from the Rayleigh-Plesset equation is one of the most popular cavitation models [15]. Similar to other cavitation models



(a) Hydraulic performance



(b) Cavitation performance under the design condition

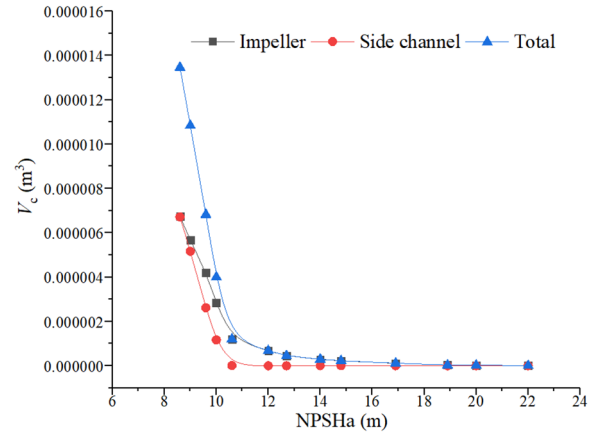
Figure 5 Performance curves of side channel pump.

in the frame of the Transport Equation Model, the Zwart model predicts the cavitation by solving the mass transfer equation for the conservation of the vapor volume fraction, which can be expressed as

$$\frac{\partial(\alpha_v \rho_v)}{\partial t} + \frac{\partial(\alpha_v \rho_v u_j)}{\partial x_j} = \dot{m}^+ - \dot{m}^-. \quad (6)$$

The source terms for the specific mass transfer rate corresponding to the vaporization \dot{m}^+ and condensation \dot{m}^- are given by

$$\dot{m}^+ = C_{\text{vap}} \frac{3\rho_v(1-\alpha_v)\alpha_{\text{nuc}}}{R_B} \sqrt{\frac{2}{3} \frac{p_v - p}{\rho_l}} (p \leq p_v), \quad (7)$$

**Figure 6** Variation of cavity volume at different NPSHa under the design condition

$$\dot{m}^- = C_{\text{cond}} \frac{3\rho_v \alpha_v}{R_B} \sqrt{\frac{2}{3} \frac{p - p_v}{\rho_l}} (p > p_v), \quad (8)$$

where p_v is the vaporization pressure of liquid, C_{vap} and C_{cond} are empirical coefficients for the different phase change processes, α_{nuc} is nucleation site volume fraction and R_B is the typical bubble size in water. These empirical constants were set to $C_{\text{vap}} = 50$, $C_{\text{cond}} = 0.01$, $\alpha_{\text{nuc}} = 5 \times 10^{-4}$ and $R_B = 1 \times 10^{-6}$ m [30].

3.4 Simulation Setup

The governing equations are discretized in the Cartesian coordinates by the finite volume method with high quality structured mesh. A high resolution was used for the advection scheme while second-order backward Euler was applied in the transient scheme. The static pressure was set as a boundary condition imposed on the inlet of the suction pipe, then a reduction in the static pressure leads to the vaporization of the vortex core. The outlet boundary condition was defined by a mass flow rate according to the simulated operating condition. Moreover, the inlet and outlet volume fraction of liquid was set as 1, while that of vapor was 0 under the cavitation condition. All physical surfaces were set as no-slip walls. As the strong unsteadiness in the side channel pump, sufficient rotations and appropriate timestep are necessary to make the internal turbulent flow fully developed and converged, which has been investigated in a previous study [26, 27]. Therefore, the timestep is 1.11×10^{-4} s for 10 rotations during transient simulations, equivalent to the time interval for the impeller to rotate by 1° [26, 27]. It is noted that the steady solution with non-cavitation flow is calculated and used as an initial condition to simulate the

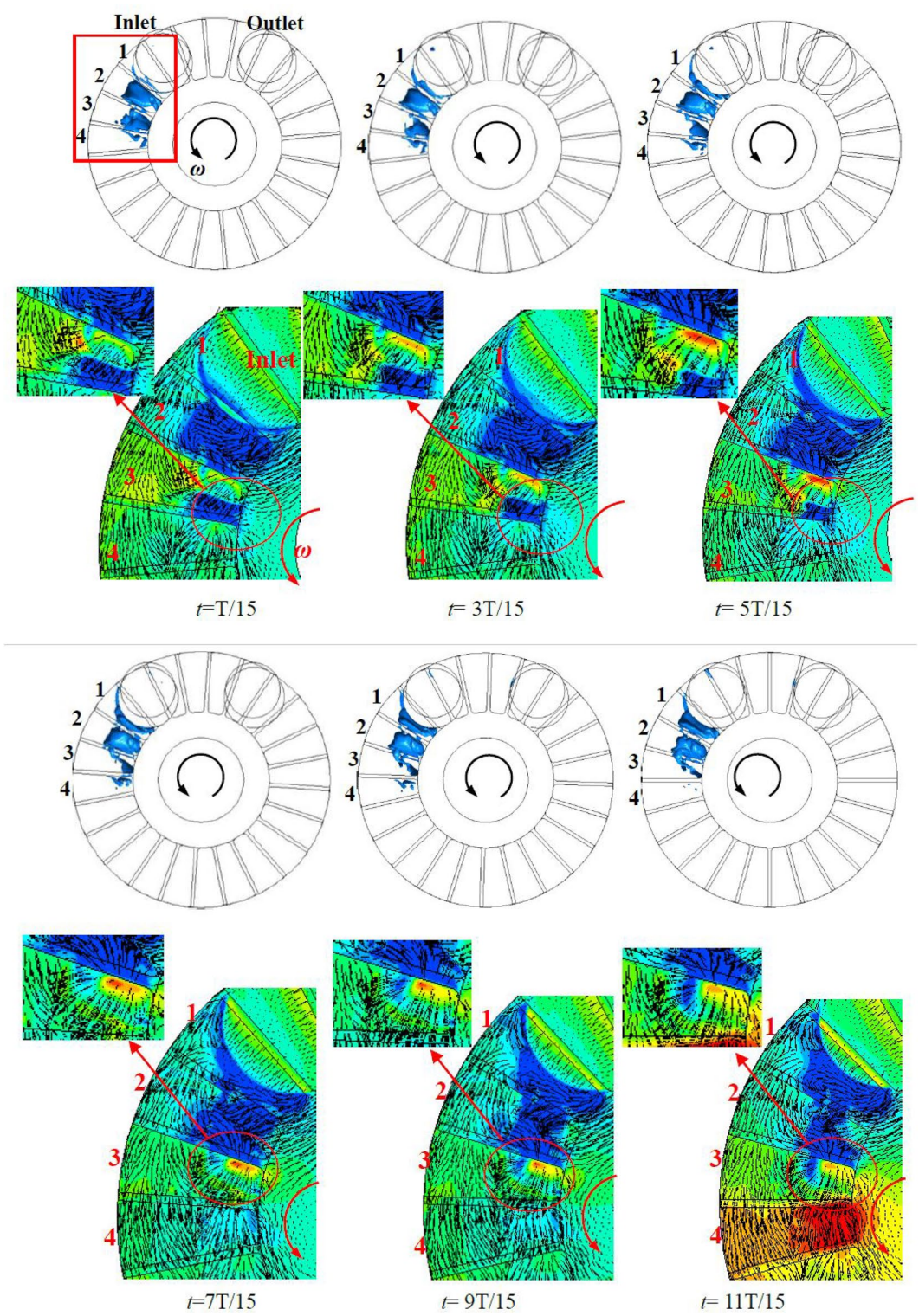


Figure 7 (continued)

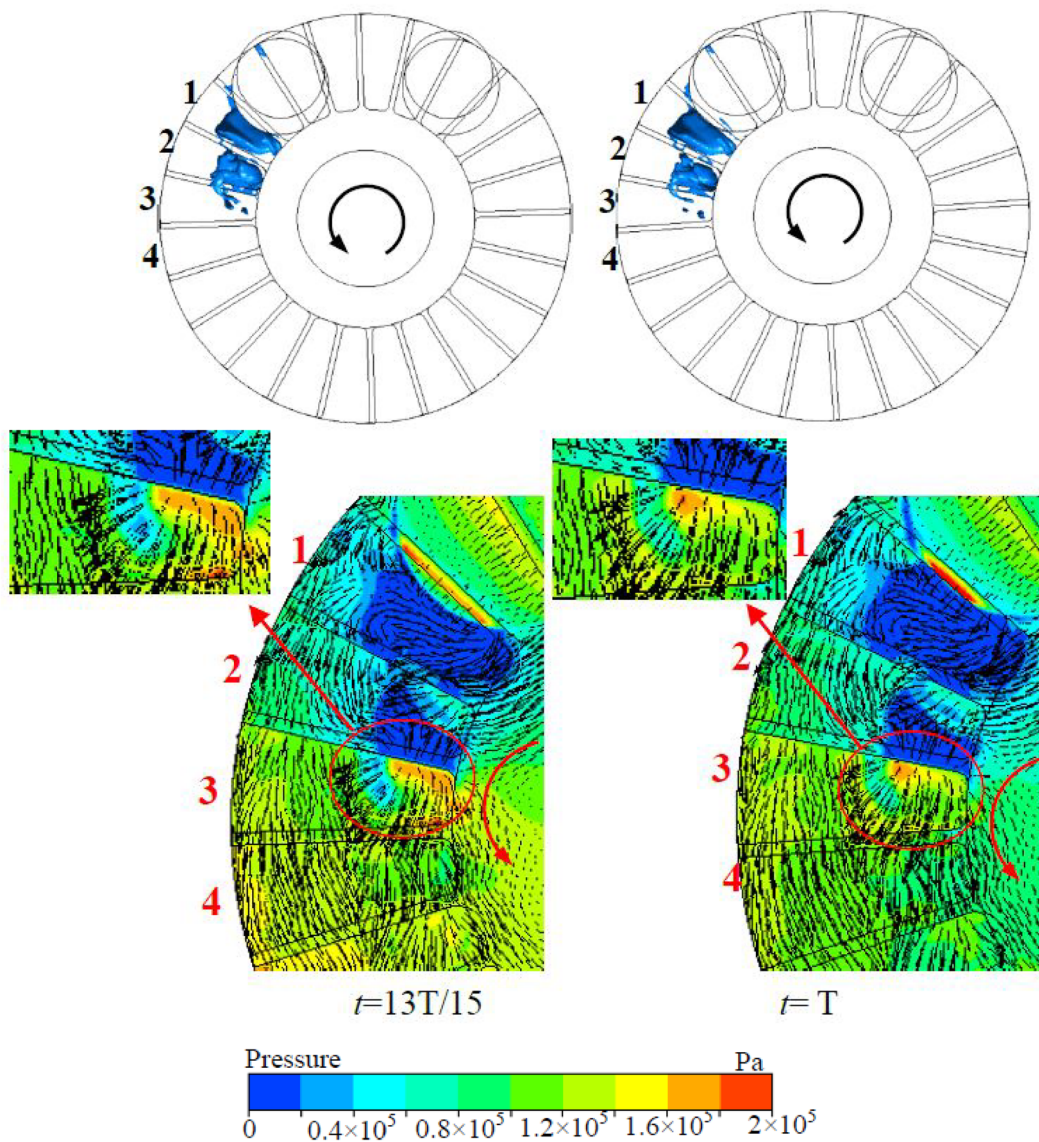


Figure 7 Evolution of vapors with impeller rotation and pressure contour with velocity vector at $NPSHa = 10.6$ m during one typical cycle

transient cavitating flow. The simulations are carried out at different $NPSHa$ and the value of $NPSHa$ is changed by the pressure of the inlet.

4 Results and Discussions

4.1 Comparison of Simulation and Measurement

The cavity structures in a similar side channel pump have been photographed by a high-speed camera [26]. This pump has the same design parameters with the model pump investigated in this study, and both two pumps have the same specific speed of 41. The main difference is that the blade suction angle of the test pump is zero, while that of the model pump is 10° . As a result, the

accuracy of numerical results for cavitating flows could be validated by comparing with those experimental observations.

Figure 4 presents the comparison of experimental photographs [26] and numerical cavity features at different Net Positive Suction Head available ($NPSHa$) under the design condition and $NPSHa$ could be calculated by

$$NPSHa = \frac{p_1 - p_v}{\rho_1 g} + \frac{v_2^2}{2g}, \quad (9)$$

where p_1 is the static pressure of the inlet, p_v is the vaporization pressure and v_2 is the outlet velocity of the pump.

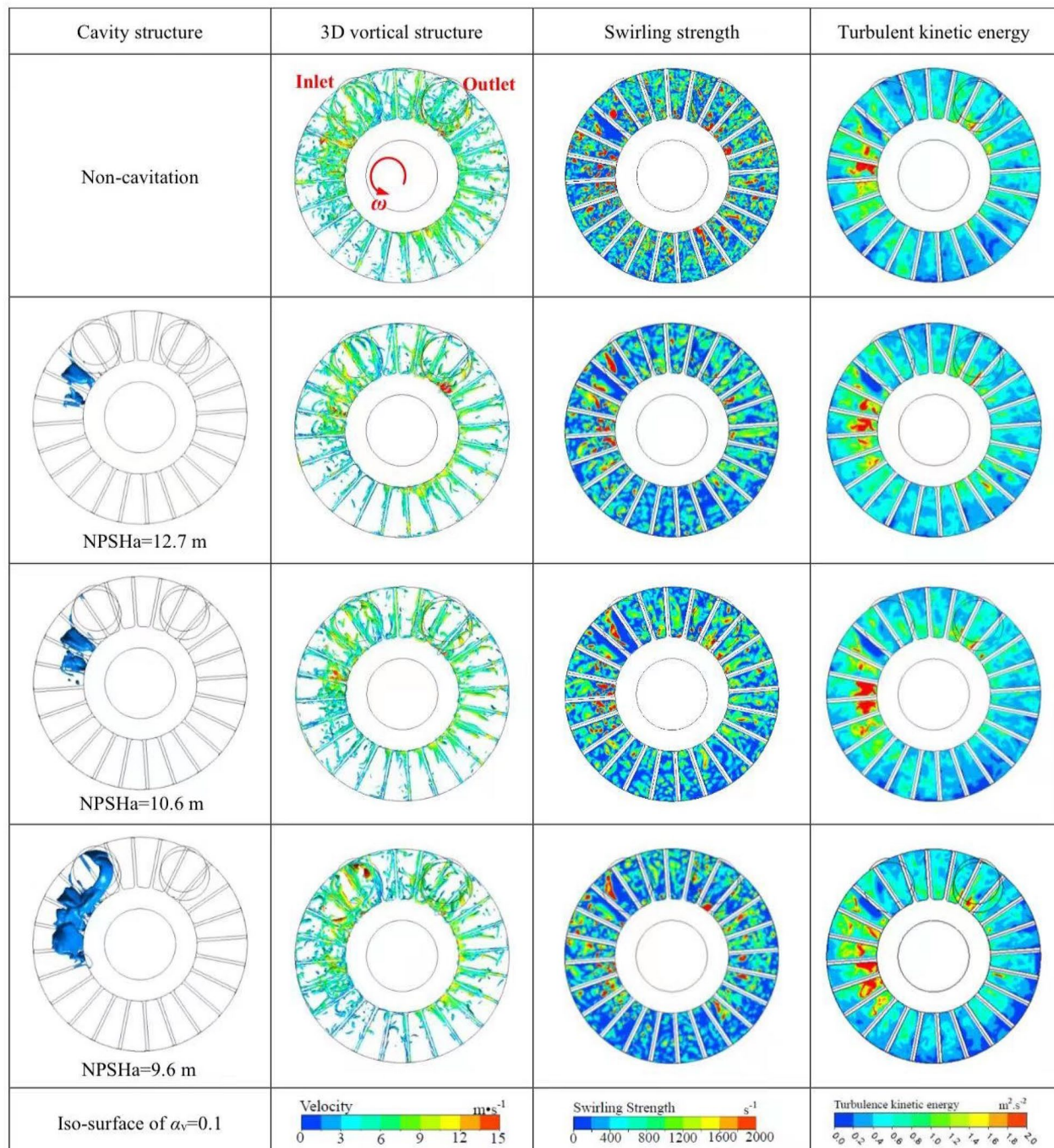


Figure 8 Distributions of cavity, vortical structures and turbulent kinetic energy at a typical instant ($t=7$) for different NPSHa

The predicted cavity shape by SAS is illustrated by the iso-surface of vapor volume fraction α_v of 0.1. It is noted that the similar impeller position with the experiment is chosen to compare the cavity structures. The location and shape of calculated vapors are consistent with experimental figures captured by high speed camera at different NPSHa. It is obvious that the vapors inside the

side channel pump firstly occur in the impeller passage near the flow entrance and attached to the region of inlet, where the pressure is lower than that of downstream. As the value of NPSHa is reduced, the vapors gradually spread to the downstream passages and more impeller passages are occupied by the cavity. Additionally, the cavities in the impeller passages mainly distribute near the

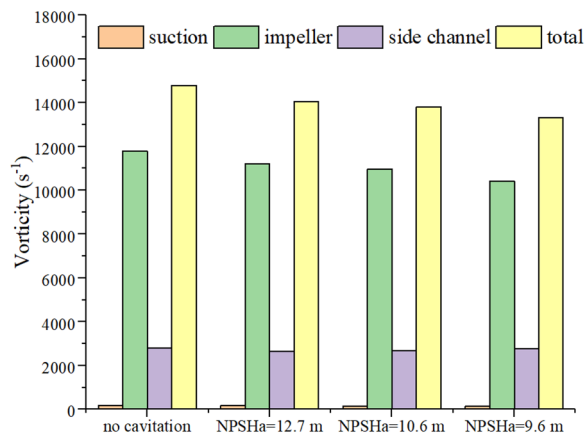


Figure 9 Values of vorticity for different cavitation numbers

hub. The vapors also appear in the side channel near the inlet and spread along the direction of rotation when the cavitation number decreases to a certain degree. Thereafter, the vapors in the impeller passages and the side channel interact with each other, resulting in the cavity developing rapidly in the side channel pump. It could even block the flow passages and the head would drop to a negative. When the value of NPSHa further decreases, the cavity structures appear in the discharge pipe and

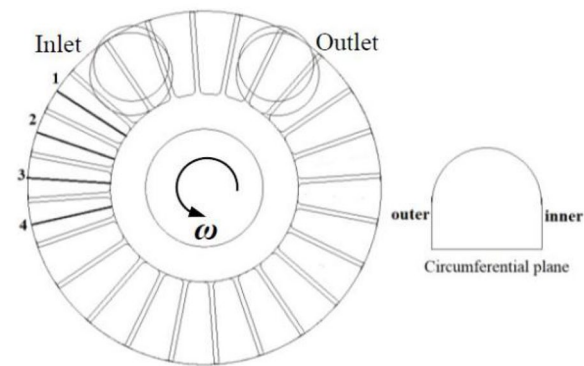


Figure 10 Positions of different circumferential planesCavitation number

form a cavitation strip, which leads to the failure of the active pump.

4.2 Performance Curves

The hydraulic and cavitation performance curves of side channel pump are plotted in Figure 5. It is obvious that the results calculated by SAS are more accurate than those of SST when compared with the experimental data. Besides, the pump heads calculated by SAS show a good agreement with the experimental data at the designed and large flow rate conditions, while a large discrepancy exists at the small flow rate condition. This

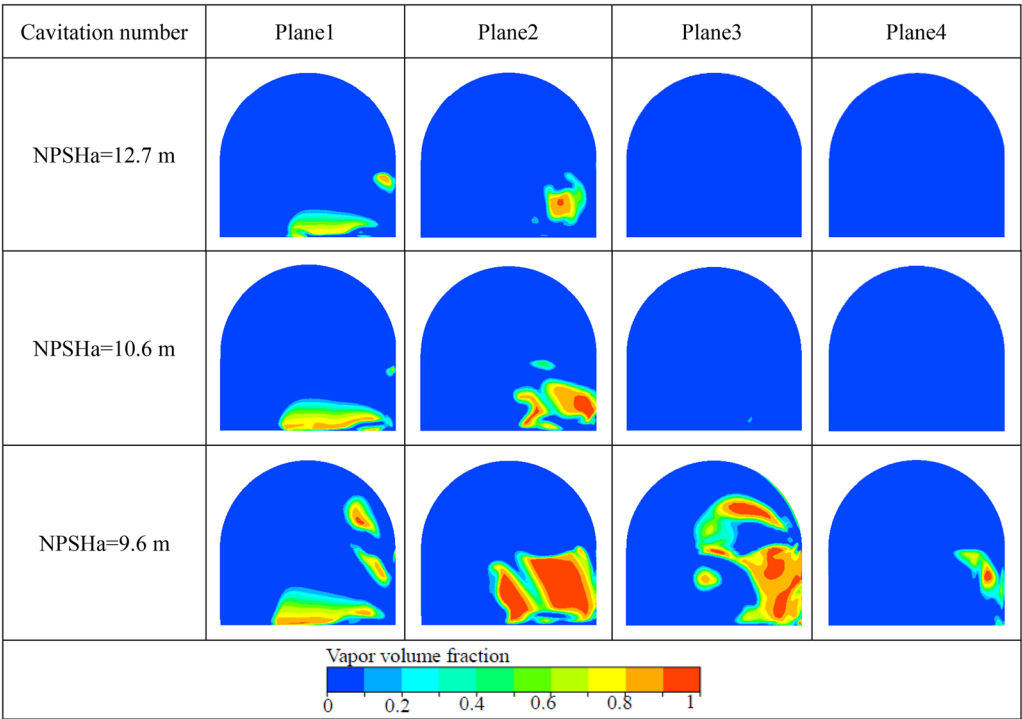


Figure 11 Contour of vapor volume fraction at a typical instant ($t = T$) for different cavitation numbers

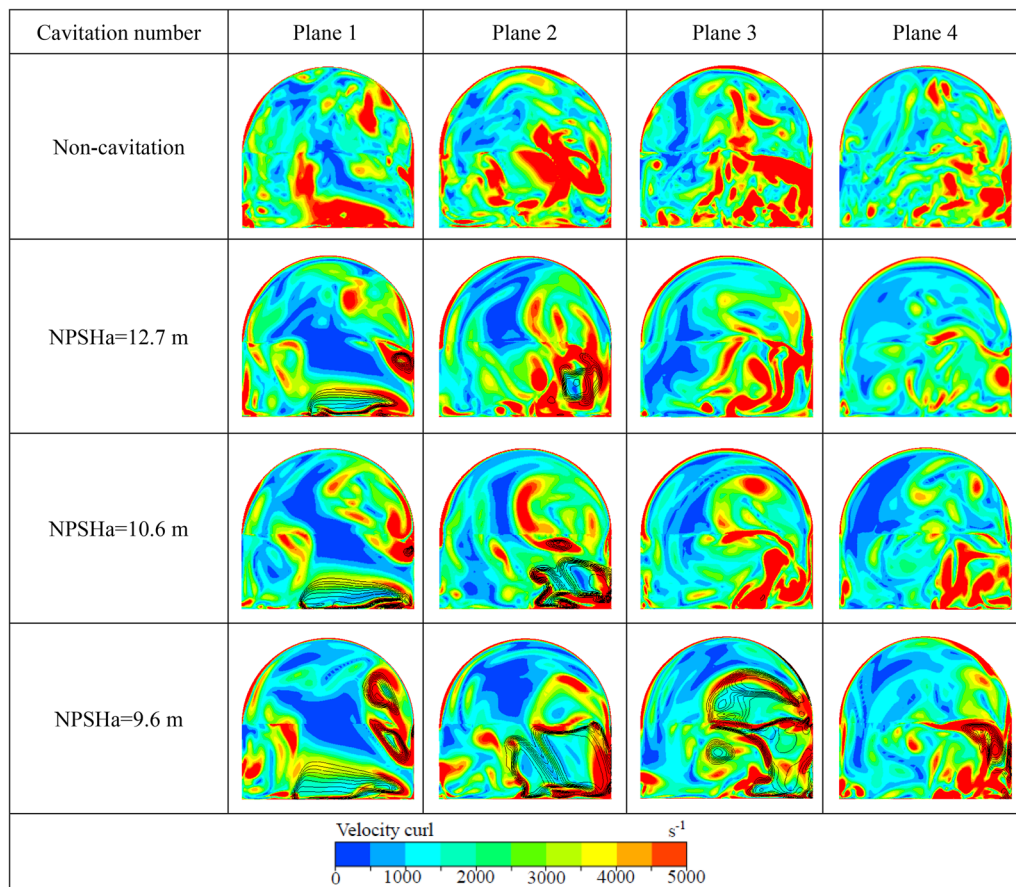


Figure 12 Contour of velocity curl at a typical instant ($t = T$) for different cavitation numbers

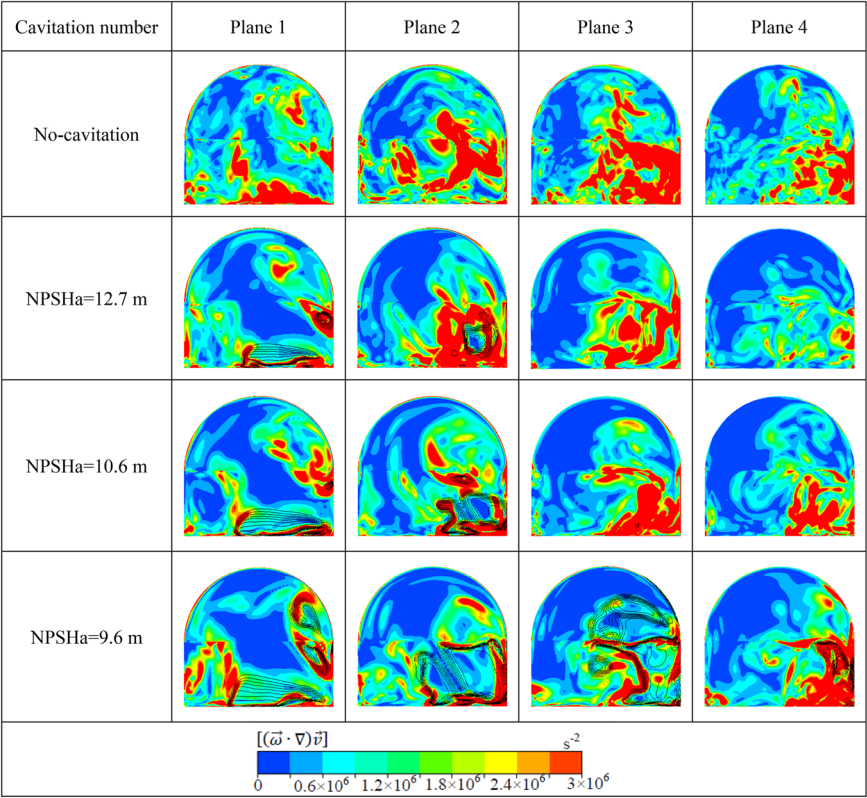
could be induced by more unsteady flows at the low flow rate, resulting in more flow losses [31]. According to the cavitation performance at the BEP condition, the value of NPSH3 is about 15.3 m. The pump head is about 12 m and starts to drop gradually after a 3% head drop with the values of NPSHa decreasing. However, the head drops rapidly after the NPSHa is reduced to 10.6 m, as marked in the red circle. Additionally, the vapors begin to propagate into the side channel, which is presented in Figure 6, leading to a rapid increase in the cavity volume and significant decrease in the head. Therefore, the further investigation on the cavitation characteristics in the paper is at this working condition of NPSHa = 10.6 m.

4.3 Evolution of Cavitating Flows

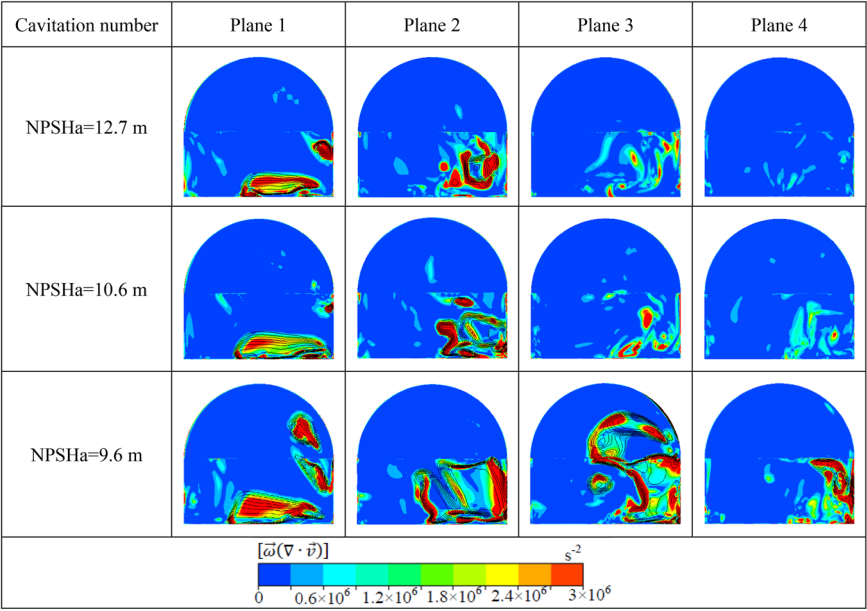
To show the time evolution of cavitation with the impeller rotation during one blade pitch (15°), eight numerical snapshots with an interval of 2° are shown in Figure 7. Meanwhile, the pressure contours with velocity vectors on the middle plane of the gap near the inlet at the corresponding instants are also depicted in Figure 7 to further

investigate the shedding behavior of cavitation in details. The initial time is defined as the moment when the pressure side of the impeller passage totally passes through the inlet and T is the time of impeller rotation during one blade pitch. The vapors are mainly distributed in the impeller passages near the inlet and the hub, occupying almost two impeller passages at NPSHa = 10.6 m. The cavity attached to the inlet keeps developing and extending from the suction surface to the pressure surface with the rotation of the impeller in Passage 1. The vapor cavities in Passage 3 and Passage 4 change to be smaller and finally collapse when moving to the higher pressure areas with the rotation of impeller. Besides, it is found that the small scale vapor structures in Passage 4 disappeared at $t = 11T/15$, which would cause the pressure increasing suddenly near the region.

Compared to pressure contours with vapor distributions, it is obvious that the regions of low pressure are consistent with the locations where the vapors are. According to the pressure distribution, it is found that a strong adverse pressure gradient is present at the end of the cavity closure region, which illustrates that the flow

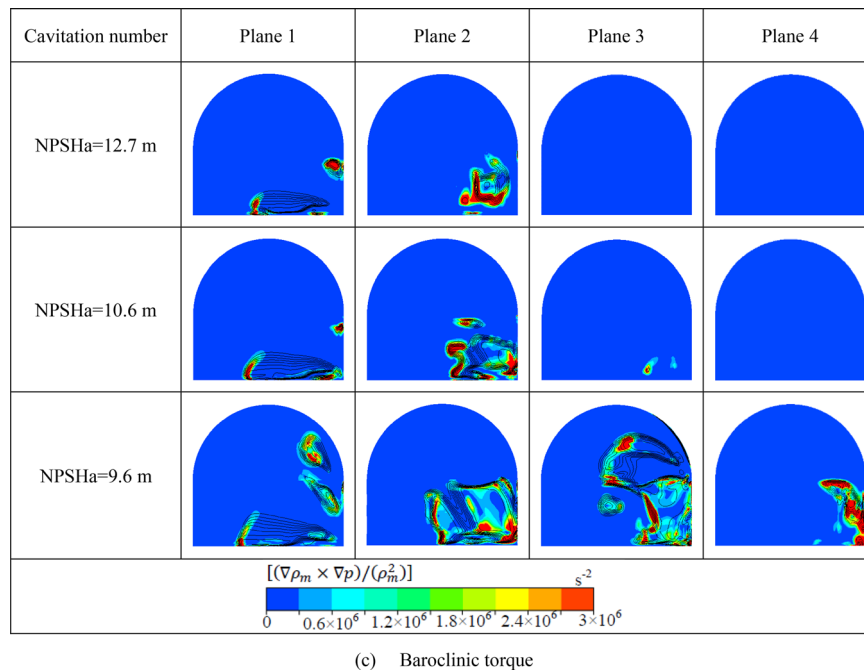


(a) Vortex stretching

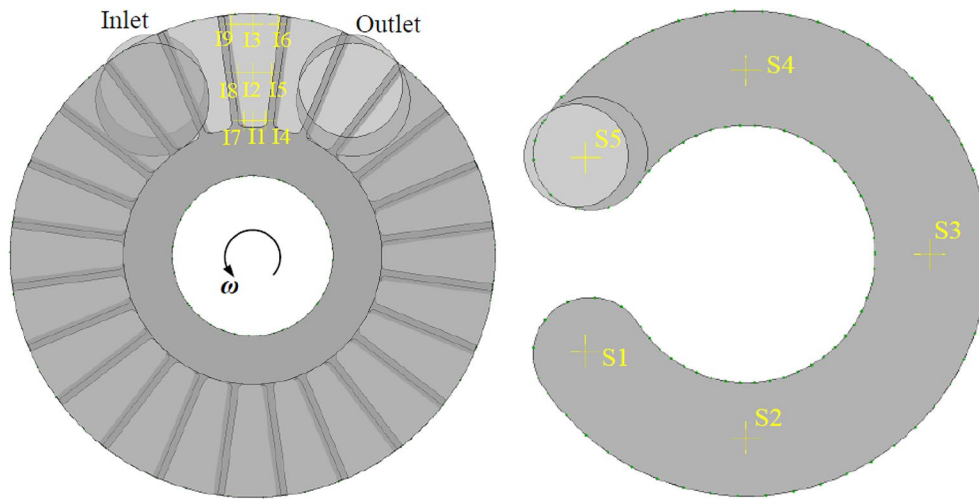


(b) Vortex dilation

Figure 13 (continued)



(c) Baroclinic torque

Figure 13 Comparison of different terms in vorticity transport equation at a typical instant ($t = T$) for different cavitation numbers**Figure 14** Positions of monitor points in the side channel pump

near the attached vapor cavity closure region is unsteady. The adverse pressure gradient is near the pressure side of Passage 3 and it forces the fluid to flow into the vapor region of Passage 2, which causes the attached cavity shedding from the wall gradually. Thereafter, the size of vapor cavity becomes smaller and collapses eventually when the cavity moves to the high pressure region downstream with the rotation of the impeller. It should

be noted that there is a sudden increase in pressure in Passage 4 at $t = 11T/15$, which is attributed to the collapse of vapors. The cavity grows and then sheds off and finally collapses during the typical cycle and this process is quasi-periodic. Thus, the shedding frequency of the cavity is similar to the blade frequency for the cavitating flow.

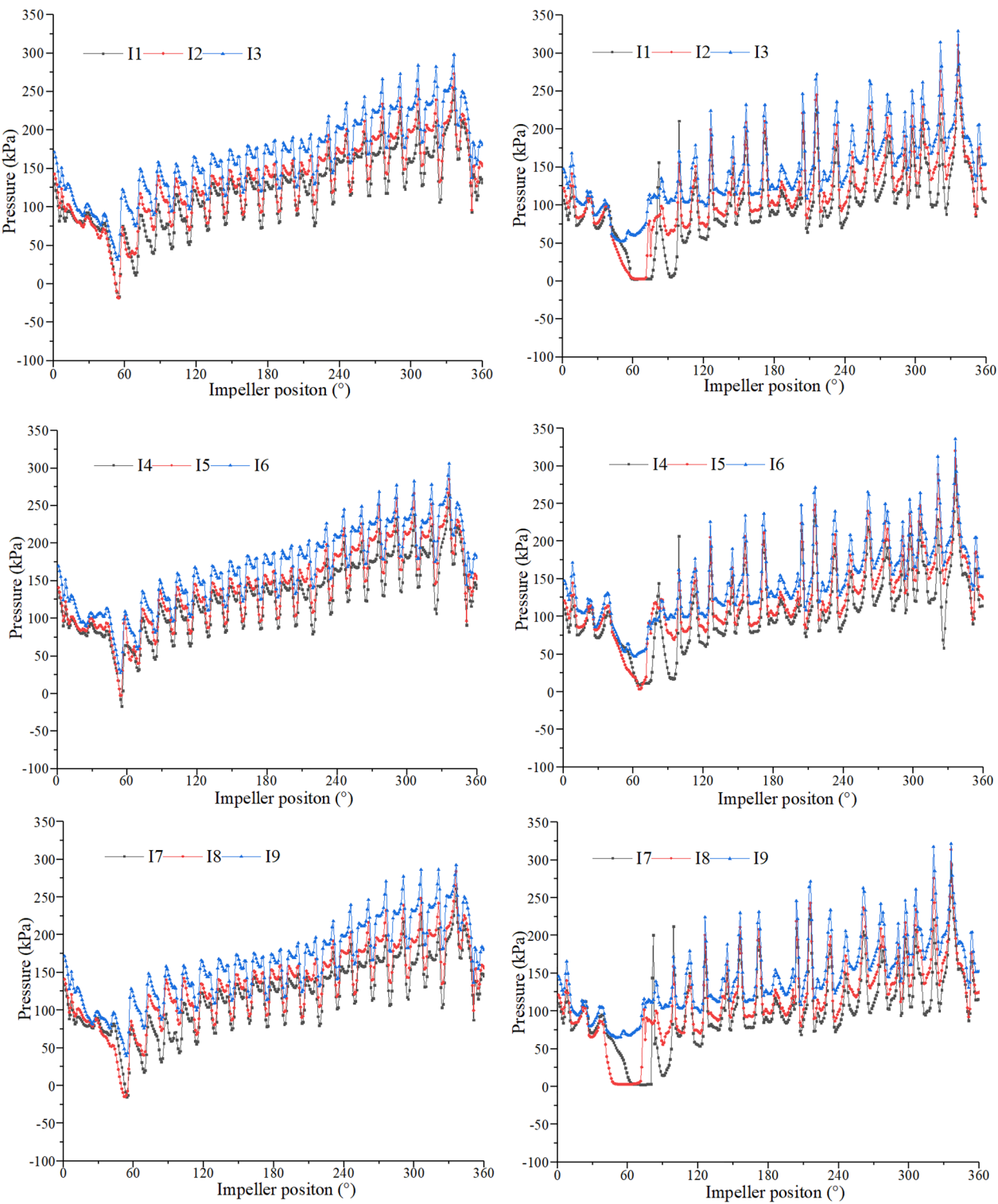


Figure 15 (continued)

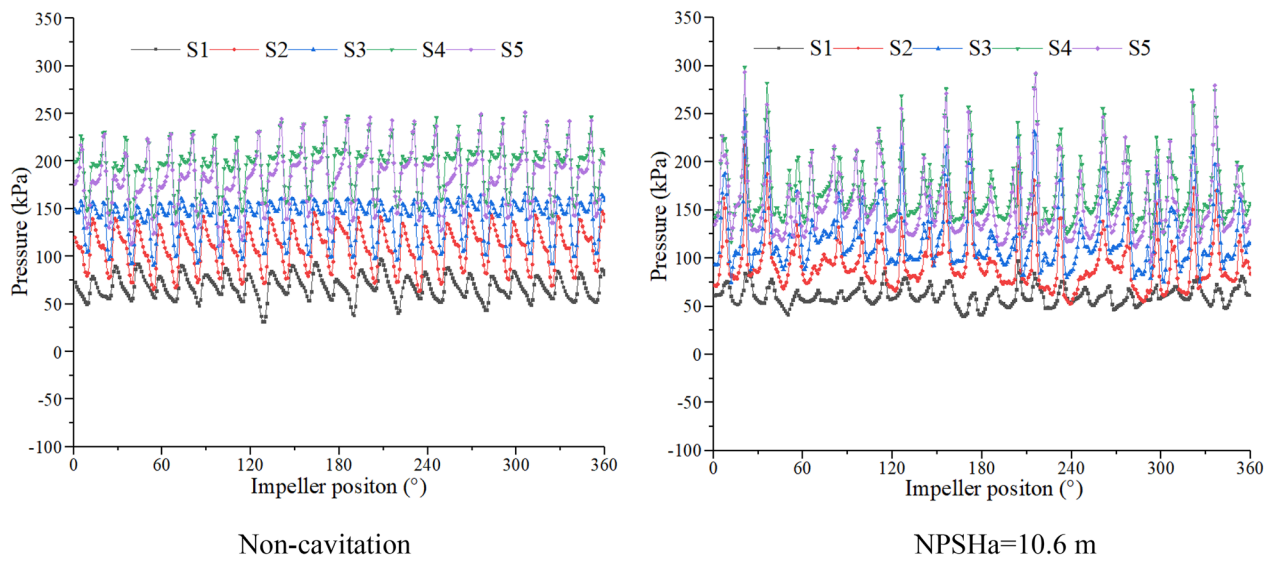


Figure 15 Pressure fluctuations in the side channel pump with time evolution

4.4 Influence of Cavitation on Vortical Structures

To reveal the vortex structures, lots of methods can be used to identify the vortex region, such as Q -criterion, λ_2 -criterion and Ω -method. The detailed analysis of the vorticity distributions for the non-cavitating flow is to verify the correlation between the cavitation and vortex. The cavity and vortical structures at different NPSHa are shown in Figure 8. Besides, the vortex core region of λ_2 -criterion is colored by the velocity, and the swirling strength and turbulence kinetic energy distributions on the middle plane of the impeller are also depicted in Figure 8. It is observed that the number of vortical structures in each flow passage reduces dramatically as the cavitation occurs and the values of vorticity at different cavitation numbers are depicted in Figure 9, which could reveal the variation of vorticity quantitatively. Meanwhile, the vortical structures in the side channel pump are influenced by cavitation development and the higher magnitude of vorticity distributes near the vapor cavity area, indicating that the vortices with low-pressure core region are easily prone to generating cavitation. In addition, the turbulent kinetic energy in the cavity region is low, but it is higher in the downstream region of the cavity than other areas and it increases obviously when compared with that under the non-cavitation condition. Therefore, it is necessary to further investigate the interactions between vapors and turbulent flows, which mainly involves complex interactions between phase-change and vortex structures [19, 20]. By comparison, it can be confirmed that cavitation promotes the vortex production and flow unsteadiness.

In order to better understand the mechanism of interactions between cavitation and vortex, the vorticity transport equation in various densities is applied in the cavitating flow as follows:

$$\frac{D\vec{\omega}}{Dt} = (\vec{\omega} \cdot \nabla) \vec{v} - \vec{\omega} (\nabla \cdot \vec{v}) + \frac{\nabla \rho_m \times \nabla p}{\rho_m^2} + (v_m + v_t) \nabla^2 \vec{\omega}, \quad (10)$$

where $\vec{\omega}$ is the vorticity, \vec{v} is the velocity, ν is the kinematic viscosity, the subscripts of m and t represent the mixture phase and turbulent respectively, ∇ is the Hamiltonian operator. In Eq. (10), the term on the left side is the rate of vorticity and each term on the right side represents the vortex stretching, vortex dilatation, baroclinic torque and viscosity diffusion in turn. The first term represents the vortex stretching by velocity gradients. The second is introduced by volumetric expansion or contraction of the fluid due to local density changes. The third is the generation of vorticity due to misaligned pressure and density gradients. The last viscous diffusion term indicates the rate of vorticity changed by the viscous diffusion. It is noted that the viscous diffusion term can be ignored with a higher Reynolds number [32], and the order of magnitude is about 10^5 near the inlet in the side channel pump. Therefore, the influence of cavitation on the vorticity distribution could be demonstrated by the contribution of vortex stretching, vortex dilatation and baroclinic torque terms. Due to the three-dimensional unsteady flows in side channel pump, the magnitudes of different terms in the vorticity transport equation are calculated to examine the influence of cavitation on vortex

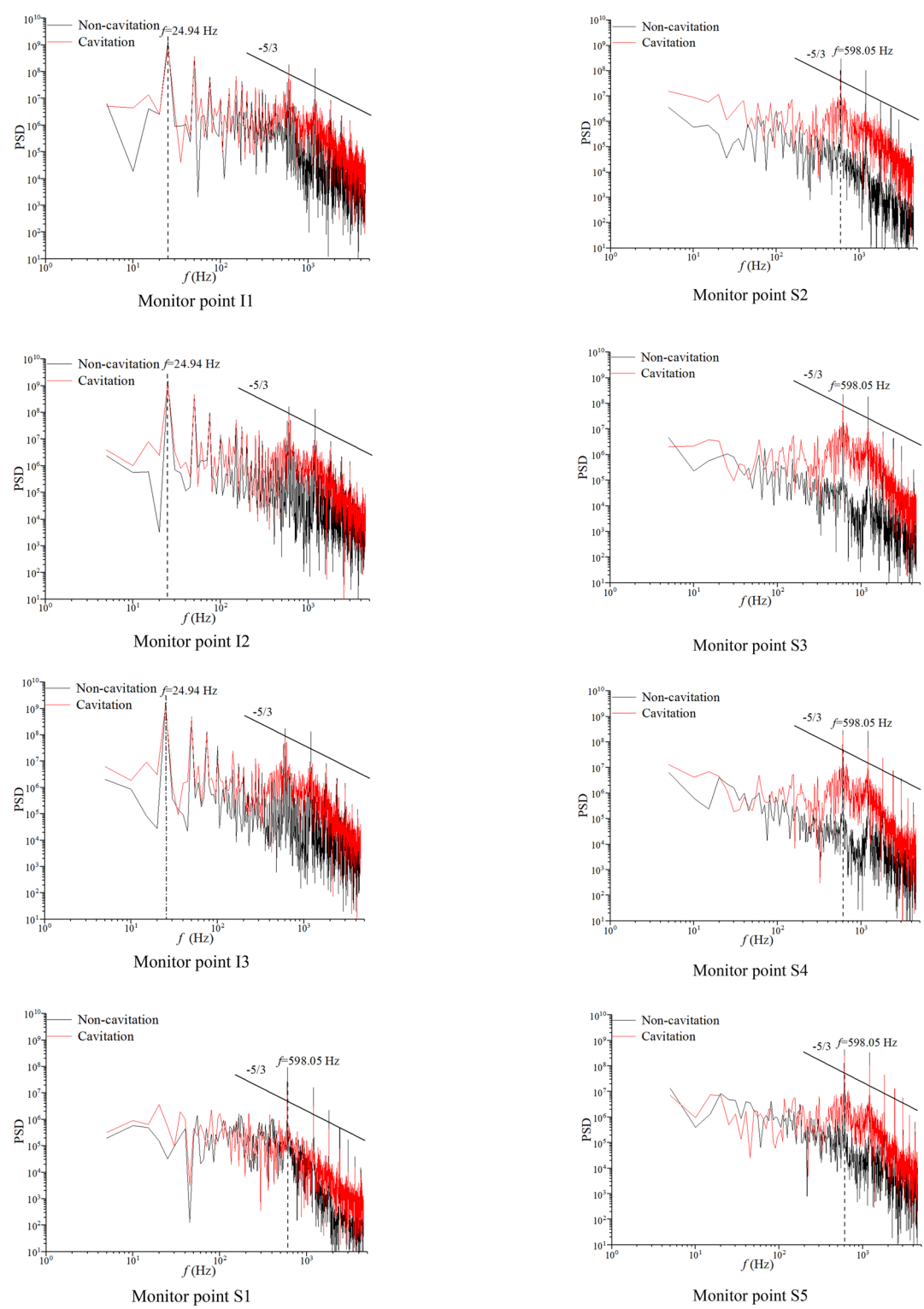


Figure 16 Power spectrum of pressure fluctuations

production. Besides, the dilatation and baroclinic torque terms are identically zero in a non-cavitating flow.

There are numerous vortices in different sizes and directions in the side channel pump and the circumferential vortex is critical to the flow exchange between impeller and side channel. Therefore, the circumferential planes at the middle of the four impeller passages near the inlet are selected for this investigation and the positions are depicted in Figure 10. The contours of vapor volume fraction at a typical instant ($t = T$) for $NPSHa = 12.7$ m, $NPSHa = 10.6$ m and $NPSHa = 9.6$ m are depicted in Figure 11. It illustrates that the vapor cavity in the passage near inlet attaches to the wall, while it sheds gradually from the surface near the cavity closure region as a result of the adverse pressure gradient. Afterwards, the cavity collapses in the high pressure region, which is consistent with the analysis above. The in-plane vorticity contours under non-cavitating and cavitating conditions are plotted in Figure 12. Besides, the contour lines of vapors (in black) are also depicted in Figure 12 to represent the positions of cavity. It is found that the vortical structures are affected significantly by the cavitation development, which suggests that cavitation might be an important mechanism for vorticity generation in cavitating flows.

Figure 13 presents the distributions of the vortex stretching, vortex dilatation and baroclinic torque terms on the circumferential planes at a typical instant ($t = T$). Similarly, the positions of cavity are depicted by the contour lines of vapors (in black) in Figure 13. These results are used to analyze the influences of the cavitation development on the vorticity production. By comparing these three terms with the vapor volume fraction and vorticity distributions, it reveals that the stretching term is dominant and responsible for the vorticity production and evolution in the cavitating flow. It is obvious that magnitudes of the stretching term decrease once the cavitation occurs, especially inside the cavity regions. It indicates that the vorticity in the cavity region is suppressed by the formation of vapors. Belahadji et al. [33] suggested that the presence of vapors in the cores of such vortices modifies the vortex stretching process by decoupling the rate of vortex straining from the rotation rate. Furthermore, as the conservation of momentum, the vortex stretching should increase the rotation rate and decrease the pressure at the vortex core in the non-cavitation case, while the pressure in the core remains constant in the cavitating flow and the vortex stretching only generates more vapors [34]. The distributions of the dilatation term illustrate that the vortex dilatation is important during the cavitating flow, whose magnitude is about the same as the stretching term. It should be noted that the values of dilatation are high in the cavity region and increase

with the decrease of $NPSHa$. Therefore, the formation and development of the vapor cavity are responsible for the increasing dilatation term. According to the distributions of the baroclinic torque, it is found that this term is mainly concentrated along the liquid and vapor interface and is negligible inside the cavity. Also, it was noted that, there was a substantial increase in the baroclinic torque as the value of $NPSHa$ decreased. Even though the magnitude of the baroclinic torque term is smaller than the vortex stretching and dilatation terms, it is important for the vorticity production along the cavity surface and near the cavity closure region, where density and pressure gradients are high.

4.5 Pressure Fluctuations

To study the effect of cavity on pressure fluctuations in the side channel pump, fourteen different points in the impeller passage and side channel have been selected. As shown in Figure 14, nine points are located in the middle plane of the impeller from the pressure side to the suction side and five points are located in the central plane and near the wall of side channel.

The time evolution of pressure fluctuations on different monitor points in the side channel pump is illustrated in Figure 15 and the initial time is the same as that in Figure 14. It is found that pressure in the impeller passage presents irregular pulsation near the inlet and outlet regions and then it tends to be regular away from these positions at the non-cavitation condition, which is probably induced by the sudden change of flow direction. Compared the pressure fluctuations of non-cavitation with those of $NPSHa = 10.6$ m, it is obvious that the existence of the vapors significantly enhances the pulsations in the impeller passage and the pressure fluctuations become irregular, especially near the inlet and inner radius of the impeller. This can be attributed to the fact that, the vapors are mainly distributed near the inner side in several downstream impeller passages of the inlet at $NPSHa = 10.6$ m. The pressure fluctuations in the side channel are regular at the non-cavitation condition, while the intensity of pulsation becomes stronger due to the cavitation, especially the points near the cavity region and downstream of the vapors.

The fast Fourier transform (FFT) is used to analyze the frequency domain of pressure fluctuations. Figure 16 shows the power spectrum of pressure fluctuations on the monitor point I1, I2, I3 and S1, S2, S3, S4, S5. According to the Kolmogorov theory [35], a range with $-5/3$ slope exists in the turbulent energy spectrum of high Reynolds number flow. The results of power spectrum density (PSD) show that the hybrid model of SAS could predict a distinct range about $-5/3$ slope, which indicates that the simulation can capture and resolve a large amount of

turbulence kinetic energy behaving like the LES mode in the outer region where the turbulent flows are dominant. The PSD results of the monitor points in the middle of the impeller passage illustrate that the primary frequency is 24.94 Hz, which is quite close to the shaft frequency of 25 Hz ($f_{\text{shaft}} = 1/n = 25$ Hz). Noted that the PSD results of points near the pressure and suction sides are similar to those points in the middle. Meanwhile, the primary frequency of monitor points in the side channel is 598.05 Hz, which is about equal to the blade frequency of 600 Hz ($f_{\text{blade}} = Z/n = 600$ Hz). It indicates that the frequency of pressure fluctuations in the side channel is related to the number of fluid exchanges in the impeller and side channel. Additionally, the results of PSD also illustrate that both pressure fluctuations in the impeller and the side channel tend to be stronger for the cavitating case (NPSHa = 10.6 m).

5 Conclusions

In this paper, unsteady cavitating turbulent flow in the side channel pump was simulated by SAS coupled with the Zwart cavitation model. The interaction between cavitation and vortical flow is firstly discussed and analyzed in the side channel pump, which may provide a better understanding of vortex cavitation in the side channel pump and is helpful to improve its cavitation performance. Based on the present investigation, the following conclusions can be drawn.

- (1) The vapors inside the side channel pump firstly occur in the impeller passage near the flow entrance and attach to the region of inlet and the vapors spread gradually to the downstream passages with the decrease of cavitation number. It is also found that a strong adverse pressure gradient is present at the end of the cavity closure region, which leads to cavity shed from the wall. The vapor cavities change to be smaller and finally collapse when moving to the higher pressure area with the rotation of impeller. The shedding frequency of cavity in the side channel pump is similar to the blade frequency.
- (2) The small scale vortices in each passage reduce significantly and gather into larger vortices due to the cavitation. Meanwhile, the evolution of vortical flow is influenced by cavitation development and a higher magnitude of vorticity distributes near the vapor cavity area. By comparing three terms of the vorticity transport equation with the vapor volume fraction and vorticity distributions, it indicates that the stretching term is dominant and responsible for the vorticity production and evolution in the cavitating flow. In addition, the magnitudes of the

stretching term decrease once the cavitation occurs, especially inside the cavity regions. It is also found that the vorticity in the cavity region is suppressed by the formation of vapors. However, the values of dilatation are high in the cavity region and increase with the decreased cavitation number. Therefore, the formation and development of the vapor cavity are responsible for the increasing dilatation term. Even though the magnitude of the baroclinic torque term is smaller than the vortex stretching and dilatation terms, it is important for the vorticity production along the cavity surface and near the cavity closure region, where density and pressure gradients are high.

- (3) According to the pressure fluctuations in the side channel pump, it is obvious that the existence of the vapors enhances the pressure fluctuations, especially near the inlet region and inner regions. The primary frequency of pressure fluctuations in the impeller is quite close to the shaft frequency of 25 Hz, while that in the side channel is about equal to the blade frequency of 600 Hz.

Acknowledgements

The authors express their sincere gratitude to Prof. Martin Böhle of the SAM in Technical University of Kaiserslautern, Germany for his great support during this work.

Author Contributions

YW was responsible for writing the entire paper and conducting the simulations. FZ and SY reviewed the paper and provided some advice on revising the paper. KC and FH provided some suggestions on the simulation. DA gave some help of language modification. All authors read and approved the final manuscript.

Authors' Informations

Yefang Wang, born in 1991, is currently a PhD candidate at *National Research Center of Pumps, Jiangsu University, China*.

Fan Zhang, born in 1987, is currently an associate professor at *National Research Center of Pumps, Jiangsu University, China*. His research interest is internal flow in vane pumps.

Shouqi Yuan, born in 1963, is currently a full professor at *National Research Center of Pumps, Jiangsu University, China*.

Ke Chen, born in 1996, is currently a PhD candidate at *National Research Center of Pumps, Jiangsu University, China*.

Feng Hong, born in 1988, is currently a lecturer at *College of Mechanical & Power Engineering, China Three Gorges University, China*.

Desmond Appiah, born in 1986, is currently a PhD post at *National Research Center of Pumps, Jiangsu University, China*.

Funding

Supported by National Natural Science Foundation of China (Grant No. 52279086) and Yunnan Provincial Ranking the Top of the List for Science and Technology Projects of China (Grant No. 202204BW050001).

Competing Interests

The authors declare no competing financial interests.

Received: 11 April 2021 Revised: 12 July 2022 Accepted: 6 January 2023
Published online: 20 February 2023

References

- [1] T Meakhail, M El-sallak, M A Serag-Eldin, et al. *Effect of guide blades fixed in the side channel on performance of peripheral pumps*. Cairo: Cairo University, 1996.
- [2] J W Song, A Engeda, M K Chung. A modified theory for the flow mechanism in a regenerative flow pump. *Proceedings of the Institution of Mechanical Engineers, Part A: Journal of Power and Energy*, 2003, 217(3): 311–321.
- [3] M Böhle, T Müller. Evaluation of the flow inside a side channel pump by the application of an analytical model and CFD. *Fluids Engineering Division Summer Meeting*, 2009, 43727: 11–18.
- [4] F Zhang, D Appiah, K Chen, et al. Dynamic characterization of vortex structures and their evolution mechanisms in a side channel pump. *ASME Journal of Fluids Engineering*, 2020, 142(11): 111502.
- [5] F Zhang, K Chen, D Appiah, et al. Description of unsteady flow characteristics in a side channel pump with a convex blade. *ASME Journal of Fluids Engineering*, 2021, 143(4): 041201.
- [6] S S Yang, F Y Kong, X Y Qu, et al. Influence of blade number on the performance and pressure pulsations in a pump used as a turbine. *Journal of Fluids Engineering*, 2012, 134(12).
- [7] C E Brennen. A review of the dynamics of cavitating pumps. *Journal of Fluids Engineering*, 2013, 135(6).
- [8] Y X Fu, J P Yuan, S Q Yuan, et al. Numerical and experimental analysis of flow phenomena in a centrifugal pump operating under low flow rates. *Journal of Fluids Engineering*, 2015, 137(1).
- [9] G C Lu, Z G Zuo, Y K Sun, et al. Experimental evidence of cavitation influences on the positive slope on the pump performance curve of a low specific speed model pump-turbine. *Renewable Energy*, 2017, 113: 1539–1550.
- [10] O Coutier-Delgosha, J L Reboud, Y Delannoy. Numerical simulation of the unsteady behaviour of cavitating flows. *International Journal for Numerical Methods in Fluids*, 2003, 42(5): 519–530.
- [11] L Tan, B S Zhu, S L Cao, et al. Cavitation flow simulation for a centrifugal pump at a low flow rate. *Science Bulletin*, 2013, 58(8): 949–952.
- [12] M Ennouri, H Kanfoudi, A B Taher, et al. Numerical flow simulation and cavitation prediction in a centrifugal pump using an SST-SAS turbulence model. *Journal of Applied Fluid Mechanics*, 2019, 12(1): 25–39.
- [13] R F Kunz, D A Boger, D R Stinebring, et al. A preconditioned Navier–Stokes method for two-phase flows with application to cavitation prediction. *Computers & Fluids*, 2000, 29(8): 849–875.
- [14] G H Schnerr, J Sauer. Physical and numerical modeling of unsteady cavitation dynamics. *Proceedings of ICMF 2001 International Conference on Multiphase Flow*, New Orleans, USA, 2001: 1–8.
- [15] P Zwart, A G Gerber, T Belamri. A two-phase model for predicting cavitation dynamics. *Proceedings of ICMF 2004 International Conference on Multiphase Flow*, Yokohama, Japan, 2004: 1–11.
- [16] A K Singhal, M M Athavale, H Y Li, et al. Mathematical basis and validation of the full cavitation model. *Journal of Fluids Engineering*, 2002, 124(3): 617–624.
- [17] H L Liu, D X Liu, Y Wang, et al. Applicative evaluation of three cavitating models on cavitating flow calculation in centrifugal pump. *Transactions of the Chinese Society of Agricultural Engineering*, 2012, 28(16): 54–59.
- [18] G J Zhang, W D Shi, D S Zhang, et al. A hybrid RANS/LES model for simulating time-dependent cloud cavitating flow around a NACA66 hydrofoil. *Science China Technological Sciences*, 2016, 59(8): 1252–1264.
- [19] R E Arndt. Cavitation in vortical flows. *Annual Review of Fluid Mechanics*, 2002, 34(1): 143–175.
- [20] B Ji, X W Luo, R E Arndt, et al. Numerical simulation of three dimensional cavitation shedding dynamics with special emphasis on cavitation–vortex interaction. *Ocean Engineering*, 2014: 64–77.
- [21] B Ji, X W Luo, R E Arndt, et al. Large eddy simulation and theoretical investigations of the transient cavitating vortical flow structure around a NACA66 hydrofoil. *International Journal of Multiphase Flow*, 2015, 68(68): 121–134.
- [22] Y Chen, J Li, Z X Gong, et al. Large eddy simulation and investigation on the laminar-turbulent transition and turbulence-cavitation interaction in the cavitating flow around hydrofoil. *International Journal of Multiphase Flow*, 2018: 300–322.
- [23] H Y Cheng, X R Bai, X P Long, et al. Large eddy simulation of the tip-leakage cavitating flow with an insight on how cavitation influences vorticity and turbulence. *Applied Mathematical Modelling*, 2019, 77: 788–809.
- [24] Y N Zhang, K H Liu, H Z Xian, et al. A review of methods for vortex identification in hydroturbines. *Renewable and Sustainable Energy Reviews*, 2017, 81(1): 1269–1285.
- [25] Q Wu, Y N Wang, G Y Wang, et al. Experimental investigation of cavitating flow-induced vibration of hydrofoils. *Ocean Engineering*, 2017, 144(1): 50–60.
- [26] S Fleder. *Mehrphasenströmung von gas-wasser-gemischen und instationäre vorgänge bei kavitation in seitenkanalpumpen*. Germany: TU Kaiserslautern, Dissertation, 2017.
- [27] Y F Wang, F Zhang, S Q Yuan, et al. Effect of URANS and hybrid RANS-LES turbulence models on unsteady turbulent flows inside a side channel pump. *ASME Journal of Fluids Engineering*, 2020, 142(6): 061503.
- [28] F R Menter, Y Egorov. The scale-adaptive simulation method for unsteady turbulent flow predictions. Part 1: theory and model description. *Flow, Turbulence and Combustion*, 2010, 85(1): 113–138.
- [29] B Chaouat. The state of the art of hybrid RANS/LES modeling for the simulation of turbulent flows. *Flow, Turbulence and Combustion*, 2017, 99(2): 279–327.
- [30] D S Zhang, L Shi, R J Zhao, et al. Study on unsteady tip leakage vortex cavitation in an axial-flow pump using an improved filter-based model. *Journal of Mechanical Science and Technology*, 2017, 31(2): 659–667.
- [31] F Zhang, D Appiah, F Hong, et al. Energy loss evaluation in a side channel pump under different wrapping angles using entropy production method. *International Communications in Heat and Mass Transfer*, 2020, 113: 104526.
- [32] B Huang, Y Zhao, G Y Wang, et al. Large eddy simulation of turbulent vortex-cavitation interactions in transient sheet/cloud cavitating flows. *Computers and Fluids*, 2014: 113–124.
- [33] B Belahadjji, J P Franc, J M Michel. Cavitation in the rotational structures of a turbulent wake. *Journal of Fluid Mechanics*, 1995: 383–403.
- [34] N Dittakavi, A Chuneekar, S Frankel. Large eddy simulation of turbulent-cavitation interactions in a venturi nozzle. *Journal of Fluids Engineering*, 2010, 132(12).
- [35] S B Pope. *Turbulent flows*. New York: Cambridge University Press, 2000.

Submit your manuscript to a SpringerOpen[®] journal and benefit from:

- Convenient online submission
- Rigorous peer review
- Open access: articles freely available online
- High visibility within the field
- Retaining the copyright to your article

Submit your next manuscript at ► [springeropen.com](https://www.springeropen.com)